(Received 29 June 2025, Accepted 29 July 2025, Scheduled 11 August 2025)

Compact Mechanically Reconfigurable DMS-BPF Filtenna with MIMO Configuration for Wide-to-Narrowband Conversion in Sub-6 GHz and X-Band Applications

Amany A. Megahed[1], Rania H. Elabd[1,2], Ahmed J. A. Al-Gburi[3,*], and Marwa E. Mousa[1]

[1] *Electronic and Communication Engineering Department, Higher Institute of Engineering and Technology, New Damietta, Egypt*
[2] *Electronic and Communication Dept., Horus University, New Damietta, Egypt*
[3] *Center for Telecommunication Research & Innovation (CeTRI), Fakulti Teknologi Dan Kejuruteraan Elektronik Dan Komputer (FTKEK), Universiti Teknikal Malaysia Melaka (UTeM), Jalan Hang Tuah Jaya, Durian Tunggal 76100, Melaka, Malaysia*

ABSTRACT: This paper introduces a novel, compact, frequency-reconfigurable multiple-input multiple-output (MIMO) filtenna that integrates a defected microstrip structure (DMS)-based bandpass filter (BPF) with a wideband circular patch antenna to support dynamic tuning across sub-6 GHz and X-band applications. The antenna operates efficiently as a wideband system while enabling mechanically controlled narrowband filtering through a reconfigurable BPF structure embedded in the feedline. Tunability is achieved using discrete switching mechanisms, allowing frequency selection from 5.9 GHz up to 12 GHz, with a peak gain of 6 dBi and high radiation efficiency. A two-port MIMO configuration with orthogonal element placement and an embedded decoupling structure ensures superior isolation (< -48 dB), extremely low envelope correlation coefficient (ECC < 0.0035), and diversity gain (DG) approaching 9.998 dB. The proposed antenna demonstrates excellent performance metrics with a compact footprint of 80×45 mm^2, making it well suited for compact wireless applications in environments with limited spectral availability.

1. INTRODUCTION

The rapid expansion of wireless communication systems and spectrum-sharing technologies has prompted the development of multifunctional antennas capable of both wideband and reconfigurable narrowband operations. Among such innovations, the concept of "filtenna" — a combination of a filter and an antenna — has attracted considerable attention due to its potential to integrate spectrum selectivity directly at the antenna front end, reducing system complexity, cost, and size [1, 2]. There is a growing need in today's wireless systems for antennas that are space-efficient, perform reliably, and support dynamic frequency tuning. Wideband antennas provide extensive spectral coverage, making them suitable for various services, yet they often lack selectivity. On the other hand, reconfigurable filtennas enable dynamic tuning across targeted frequency ranges, allowing coexistence in congested spectral environments and enhanced interference rejection [3, 4]. The integration of a DMS-based BPF into the feed line of a wideband antenna has proven to be an effective method to introduce such reconfigurability while maintaining compactness [5].

Patch and monopole antennas are often favored in conformal applications due to their simple geometries and ease of integration. Nonetheless, their relatively large physical dimensions hinder their suitability for compact or miniaturized devices [6]. To address this, various miniaturization techniques — such as embedding asymmetric stubs or slots, either open- or short-circuited — have been employed within the radiating structure. While effective in reducing size, these modifications often increase structural complexity, making fabrication more challenging [7].

In parallel, multiple-input multiple-output (MIMO) technology has become an essential strategy in modern communication systems, offering improvements in data throughput, diversity gain, and mitigation of multipath fading [8–11]. Additionally, discrete wavelet transforms (DWTs) have emerged as effective tools for enhancing spectral efficiency, especially in systems employing orthogonal frequency division multiplexing (OFDM). Their application in antenna design enables the development of diversity schemes that improve both system performance and spectral utilization [12–18].

For practical MIMO antenna implementations, two critical requirements must be met: achieving high isolation between antenna structures designed to minimize mutual coupling (MC) between elements and maintaining a compact structure suitable for portable devices. Enhanced isolation improves system performance by minimizing undesired interactions between the radiators [19]. However, as the size of the antenna array increases, the potential for MC also rises. Consequently, numerous techniques have been proposed in the literature to suppress MC [20–32].

For example, the work in [20] presents a dual-polarized MIMO system with orthogonal elements achieving 22.5 dB isolation within a compact 27×21 mm^2 footprint. In another study [22], a quad-port double-sided MIMO antenna uti-

* Corresponding author: Ahmed Jamal Abdullah Al-Gburi (ahmedjamal@ieee.org, ahmedjamal@utem.edu.my).

lizing an electromagnetic band gap (EBG) structure was developed, featuring four polygon-shaped elements and a semi-slotted ground plane on a $30 \times 30\,\text{mm}^2$ FR4 substrate. Similarly, the use of a meander-line EBG to suppress MC between two $32 \times 64\,\text{mm}^2$ antennas was explored in [23]. Furthermore, carbon black film was employed in [33] to absorb inter-element interference, resulting in improved isolation with $S_{21} < -15\,\text{dB}$ and ECC below 0.02. Despite these advancements, many existing configurations struggle to balance performance with size constraints and isolation effectiveness, highlighting the ongoing need for innovative MIMO antenna configurations.

This work presents a novel approach to designing a compact MIMO filtenna with frequency reconfigurability by combining a DMS-based BPF and a wideband antenna within a mechanically tunable framework. Unlike conventional designs that rely on positive-intrinsic-negative (PIN) or varactor diodes, this work employs mechanical switches to enable low-cost, linear frequency tuning while minimizing nonlinearity and power consumption. Furthermore, the introduction of a metamaterial-based decoupling structure significantly improves inter-port isolation without increasing system complexity. These innovations collectively result in a compact, high-performance MIMO filtenna capable of supporting sub-6 GHz and X-band communication, with superior isolation, low ECC, and high gain.

2. WIDE BAND ANTENNA DESIGN

This subsection presents the design of a wideband (WB) circular patch antenna featuring a hexagonal slot and a partial ground plane configuration, as shown in Figure 1. The antenna is fabricated on an FR4 substrate characterized by a dielectric constant (ε_r) of 4.3 and a thickness h of 1.6 mm. The structure was modeled and analyzed using Computer Simulation Technology (CST) software. Table 1 outlines the detailed dimensions of the antenna in millimeters. The width of the microstrip feeding line is W_f, and it is employed to link the patch to a $50\,\Omega$ SMA connector. The antenna design process is illustrated in three progressive stages, culminating in an optimized geometry for enhanced performance as shown in Figure 2(a). In Stage 1, the initial structure comprises a solid circular radiating element connected to a microstrip feedline, forming the base shape. Moving to Stage 2, a circular slot is etched at the center of the radiating element to create a ring-shaped configuration. This modification is intended to improve impedance matching and bandwidth characteristics. In Stage 3, a hexagonal slot is introduced inside the circular patch, further refining the current distribution and enhancing the resonant behavior of the antenna. A partial ground plane is used consistently across all stages to support wideband characteristics by improving impedance matching and minimizing back radiation. This systematic evolution of the antenna structure ensures improved performance metrics suitable for modern communication applications. Figure 2(b) displays the simulated S_{11} (return loss) performance of the three stages over a frequency range of 1 GHz to 12 GHz. Each stage exhibits distinct resonant frequencies and varying levels of return loss, indicating improvements in impedance matching and bandwidth with successive iterations. Notably, Stage 3 demonstrates the best overall return loss characteristics, suggesting excellent power transfer efficiency at this frequency. The comparative analysis of these stages is crucial for understanding the optimization process, and the study also examines how design modifications influence the antenna's behavior across its full operational bandwidth. As shown in Figure 2(b), the simulated reflection coefficient ($|S_{11}|$) is plotted versus frequency. The results demonstrate that the antenna exhibits wideband characteristics, maintaining $|S_{11}|$ values below $-10\,\text{dB}$ from 2.4 GHz up to frequencies exceeding 12 GHz.

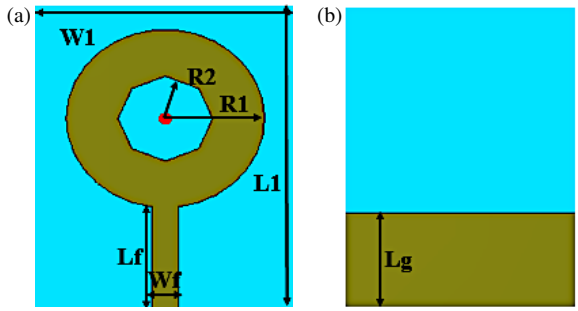

FIGURE 1. Illustration of the proposed wideband antenna: (a) front side and (b) rear side views.

TABLE 1. Sizes of the planned WB antenna in mm.

$W1$	$L1$	Lf	Lg	$R1$	$R2$	Wf
35	45	16	14.7	13	6.2	3.3999

As exposed in Figure 3(b), the antenna maintains a high simulated efficiency across the entire operating band, ranging between 80% and 99%. Furthermore, the realized gain, depicted in Figure 3(c), varies from approximately 2.2 dB to 5.9 dB over the same frequency range.

Figure 3 displays the manufactured version of the proposed wideband antenna. As shown in Figure 4(a). The results show that $|S_{11}|$ stays below $-10\,\text{dB}$ across a wide frequency range, from 2.4 GHz to beyond 12 GHz. The measured outcomes align closely with the simulated data, with slight variations primarily due to fabrication-related imperfections.

Figure 4(b) illustrates the efficiency of the proposed WB antenna. Both simulation and measurement demonstrate a high level of efficiency, generally exceeding 0.9 (90%) across much of the spectrum. There is a strong agreement between the imitation and experimental data, particularly in the lower frequency range and around 8–12 GHz, which validates the accuracy of the simulation model. A slight divergence is observable between 6 GHz and 8 GHz, where the measured efficiency dips slightly below the simulated values, indicating potential real-world losses or discrepancies not fully captured in the simulation. Figure 4(c) illustrates the gain of the planned antenna as a function of frequency, spanning from 1 GHz to 12 GHz. The curves show a general trend of increasing gain with frequency, rising from approximately $-10\,\text{dBi}$ at 1 GHz to over

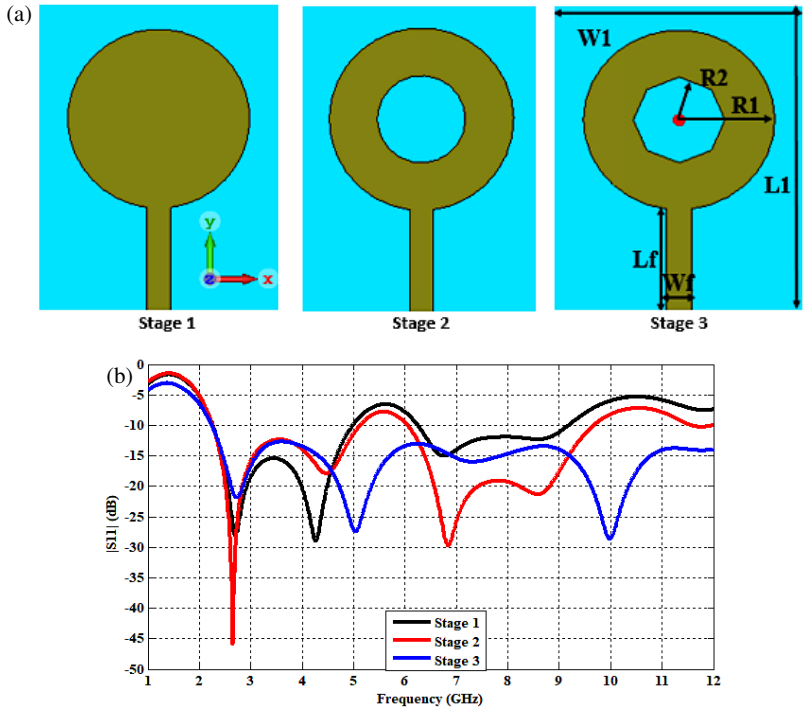

FIGURE 2. (a) Antenna design stages, and (b) S_{11} of antenna stages.

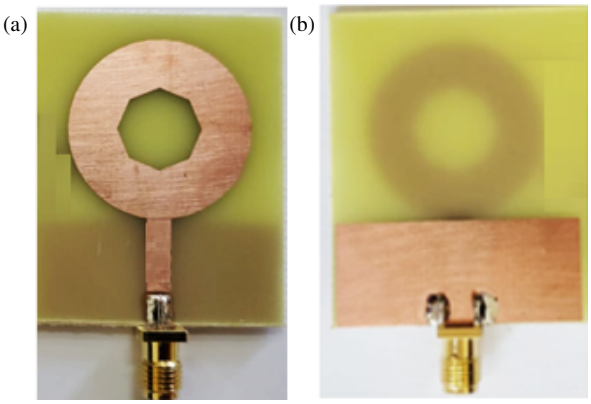

FIGURE 3. Fabricated model of the planned antenna. (a) Front side and (b) back side.

6 dBi at 12 GHz. Figure 3 illustrates the fabricated model of the planned antenna, which was produced using a conventional chemical impression technique to experimentally verify the design concept.

Figure 5 displays the measured and simulated beam patterns of a planned antenna at two distinct frequencies: (a) 5 GHz and (b) 10 GHz. For each frequency, both the H-field (azimuthal plane) and E-field (elevation plane) patterns are presented, with solid lines representing simulated data and dashed lines indicating measured data. In this work, the radiation pattern is presented using a polar coordinate system to illustrate the directional strength of the radiated signal. At 5 GHz, the measured outcomes closely align with the simulated predicted shapes for both fields, showing a clear directional lobe. Similarly, at 10 GHz, the agreement between simulation and measurement remains strong, although the beam shape appears slightly more concentrated, as expected for a higher frequency.

3. CONFIGURATION AND DESIGN OF A BANDPASS FILTER BASED ON DMS TECHNIQUE

This subsection outlines the strategy process of the proposed bandpass filter (BPF), which is implemented using the DMS technique. The design begins by etching two narrow slits at the center of the microstrip line, spaced 0.5 mm apart. These slits serve as a immovable capacitance element, as illustrated in Figure 6. Additionally, a U-shaped slot measuring $4.69 \times 0.86\,\text{mm}^2$ is introduced at the central section of the strip to regulate the electromagnetic coupling among the adjacent transmission line segments. These structural modifications enable the filter to exhibit bandpass behavior by forming a combination of parallel and series resonance paths.

The DMS can be modeled using lumped circuit elements based on conventional circuit theory. The initial strategy is simulated using CST software. To determine the individual resonant frequencies, the resulting S-parameter matrix is exported to Advanced Design System (ADS) for further analysis. As outlined in [34], the equivalent capacitance and inductance values can be derived using the following two equations.

$$C_{s,p} = \frac{f_c}{200\pi(f_o^2 - f_c^2)}, \quad L_{s,p} = \frac{1}{4\pi^2 f_o^2 C_{s,p}}$$

In this context, f_o corresponds to the resonance point, and f_c defines the filter's cut-off threshold. Variations in the capacitance C directly influence the location of the operational frequency band.

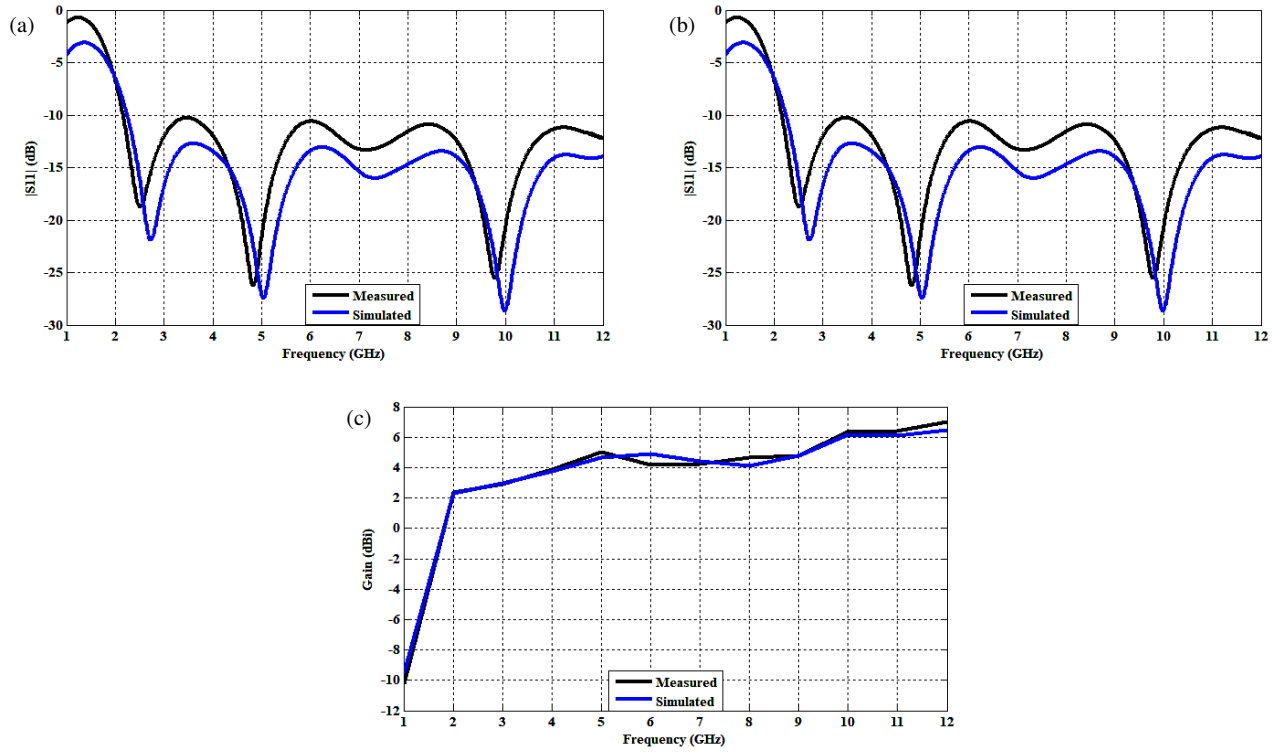

FIGURE 4. Performance of the planned wideband antenna element. (a) $|S_{11}|$, (b) efficiency, and (c) gain.

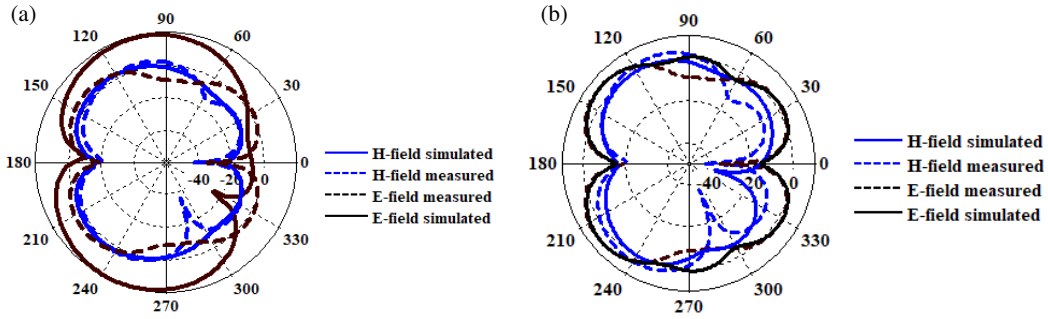

FIGURE 5. Beamforms of suggested antenna at (a) 5 GHz and (b) 10 GHz.

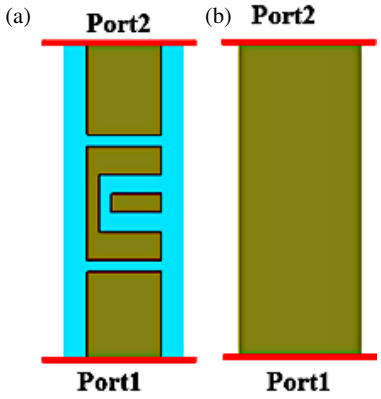

FIGURE 6. Planned DMS-BPF assembly. (a) Front sight and (b) back sight.

Figure 7 illustrates the correspondent circuit representation of the DMS-based BPF. In this model, the two etched gaps are represented by a parallel-series LC circuit composed of an inductor L_s and a capacitor C_s, while the U-shaped slot is modeled using components L_p and C_p. The simulated scattering parameters for the equivalent circuit, obtained via ADS, are shown in Figure 8(a). The results demonstrate an ideal bandpass response, allowing signal transmission at 7.6 GHz based on the specified values of inductance and capacitance L and C) illustrated in Figure 7. Figure 8(b) shows the S-parameters for the full-wave simulated DMS BPF structure, revealing that $|S_{11}|$ remains below -10 dB at 7.6 GHz, with an insertion loss of approximately -1.8 dB.

4. ADAPTIVE FILTER-ANTENNA SYSTEM WITH FREQUENCY RECONFIGURABILITY

This subsetion presents the strategy of the proposed tunable filtenna. As depicted in Figure 9, the DMS-based (BPF) is integrated into the feed line of the wideband antenna to form the filtenna structure. This configuration facilitates impedance matching between the BPF and radiating patch while also con-

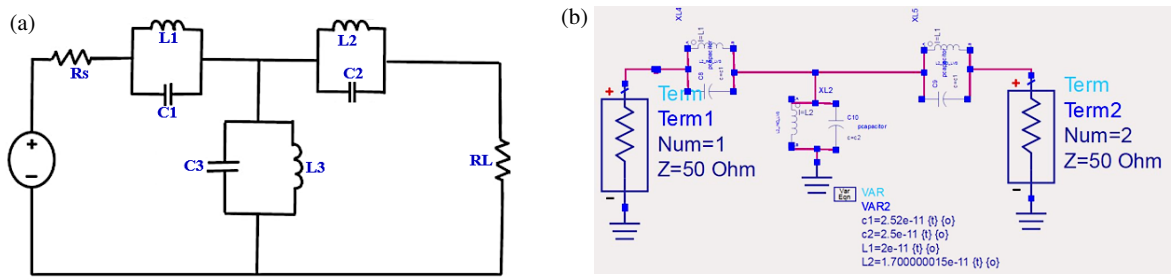

FIGURE 7. (a) Corresponding circuit typical of the reconfigurable DMS-based filter. (b) Graphic representation implemented in the ADS.

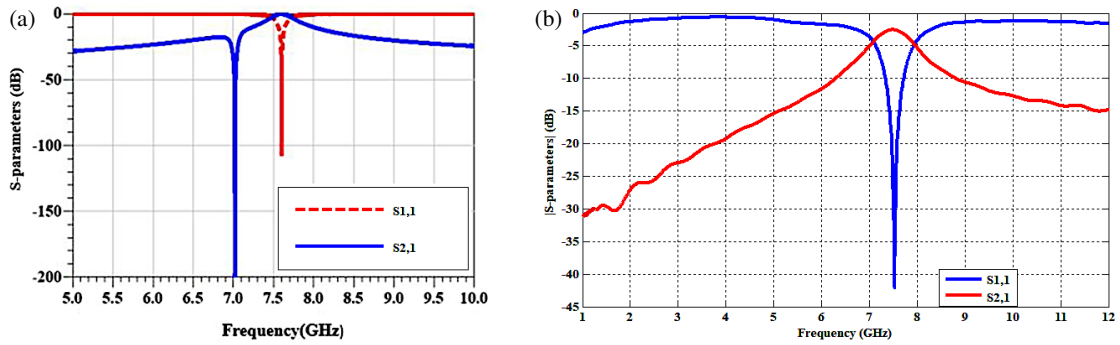

FIGURE 8. Simulated S-parameters of (a) the DMS equivalent circuit modeled in the ADS environment, and (b) the planned BPF construction created on the DMS technique.

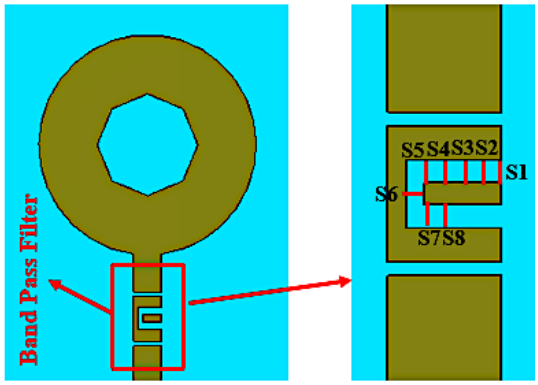

FIGURE 9. Front sight of the proposed tunable filtenna structure, illustrating the placement of multiple switching elements.

tributing to system miniaturization and cost efficiency. To enable reconfigurability and frequency tuning, eight switches are strategically positioned within the filtenna structure, as presented in Figure 9.

Figure 10(a) displays a comparison between the reflection coefficient ($|S_{11}|$) of the standalone antenna and the proposed filtenna. The integration of the BPF effectively converts the wideband antenna response into a narrowband operation with enhanced selectivity. Figures 10(b) and 10(c) further illustrate the influence of the BPF's insertion loss and also the switching states on the filtenna's efficiency and gain. Across the tuning range, the value of gain varies from 3 dBi to 5.8 dBi, while the efficiency remains around 82.4%. The filtenna configurations under different switch states are shown in Figure 11(a), and the corresponding frequency tuning range — from 5.9 GHz to beyond 11.7 GHz, totaling a bandwidth of 5.55 GHz — is displayed in Figure 11(b). Table 2 summarizes the performance metrics of the filtenna under various switch states, including operational bandwidth, 10 dB bandwidth, efficiency, and realized gain. The findings demonstrate that the proposed structure achieves strong frequency selectivity, maintaining narrow operational bandwidths between 37.7 MHz and 600 MHz across the full range of tuning configurations.

To verify the design concept, a model of the proposed filtenna was manufactured via chemical etching and tested under various switch conditions. Figure 12 illustrates its top view for each state.

To implement the switching mechanism, simple metallic screws are used as mechanical switches. These screws are manually inserted into or removed from predefined holes etched at specific locations in the DMS-based filter. When a screw is inserted, it effectively alters the current distribution and loading effect on the microstrip line, resulting in a change in the resonance frequency. This approach offers a low-cost, bias-free alternative to electronic switching and is particularly suitable for proof-of-concept prototyping and laboratory validation.

Figure 13 illustrates a comparison between the simulated and measured reflection coefficients ($|S_{11}|$) for the proposed filtenna across different switch settings. When only switch S1 is activated (Case: 00000001), the antenna exhibits resonance at 5.9 GHz, achieving a measured slight bandwidth of 2.13%, covering the range from 5.85 to 5.95 GHz. In another configuration, where switches S4 and S6 are ON while the remaining are OFF (Case: 00101000), resonance occurs at 8 GHz, with a measured impedance bandwidth ($|S_{11}| < -10$ dB) of 4.15%, spanning from 7.89 to 8.11 GHz. Additionally, when

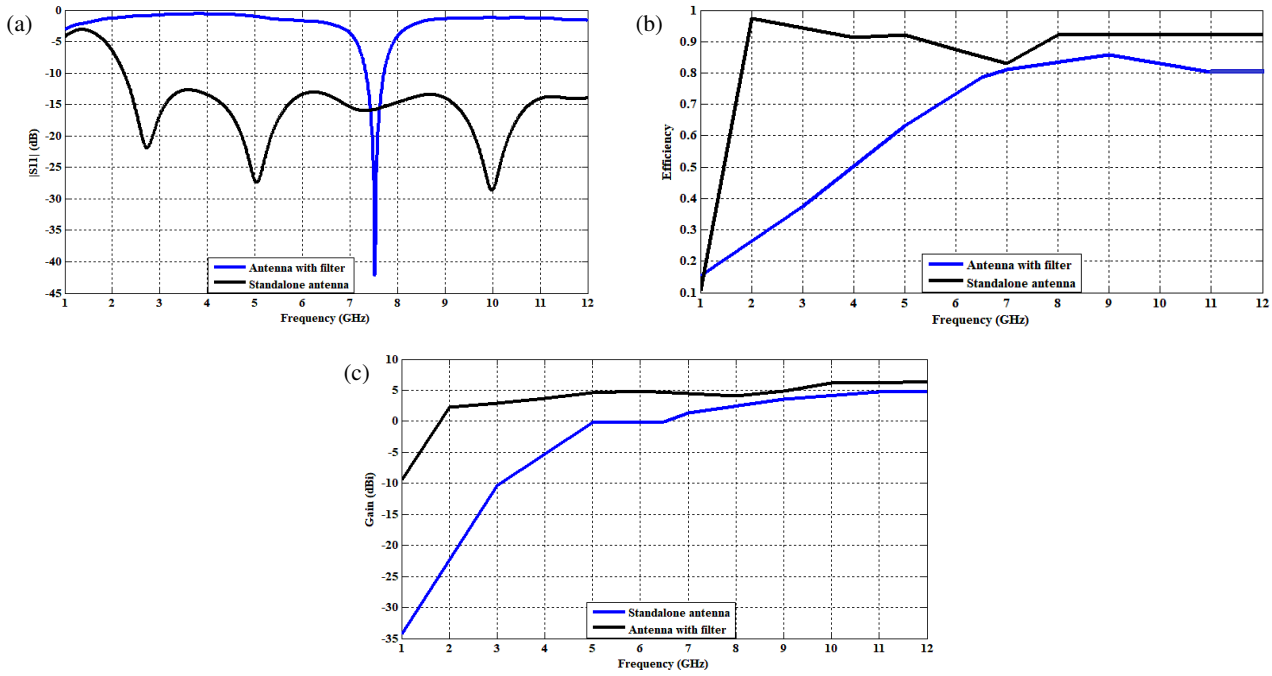

FIGURE 10. Performance of the standalone antenna compared to the antenna integrated with the filter: (a) reflection coefficient ($|S_{11}|$), (b) efficiency, and (c) gain.

TABLE 2. Operational characteristics of the suggested filtenna for different switching scenarios.

State of switches	Modes S8, S7, S6, S5, S4, S3, S2, S1	Frequency of resonance (GHz)	Bandwidth (GHz)	10 dB BW (MHz)	Efficiency (%)	Gain (dB)
All off	00000000	7.578	7.4–7.75	37.7	82	3
S1 on	00000001	5.9	5.85–5.95	100	80.6	3.8
S2 on	00000010	6.14	6.02–6.26	240	81.1	3.9
S3 on	00000100	6.34	6.22–6.46	240	71.5	3.7
S4 on	00001000	6.56	6.45–6.68	230	74.0	4.46
S5 on	00010000	6.8	6.64–6.96	320	69.6	4.2
S6 on	00100000	7	6.85–7.15	300	71.8	3.77
S7 on	01000000	7.17	6.97–7.37	400	76.2	3.9
S8 on	10000000	7.6	7.4–7.8	400	80.2	4.1
S4, S6	00101000	8	7.89–8.11	220	82.4	4.3
S5, S7 on	01010000	8.4	8.17–8.63	460	72.9	5.7
S1, S7 on	01000001	8.7	8.45–8.95	500	72.5	5.6
S2, S7 on	01000010	9.1	8.87–9.33	460	70.5	5.8
S1, S8 on	10000001	9.6	9.3–9.9	600	79.5	3.02
S2, S8 on	10000010	10.7	10.44–10.96	520	80.5	3.8
S5, S6 on	00110000	11.2	10.98–11.42	440	81	3.9

A logic value of '1' indicates that the switch is turned ON, whereas '0' indicates it is OFF.

both S1 and S7 are ON and all other switches are OFF (Case: 01000001), the antenna operates at 8.7 GHz.

Overall, a strong agreement is observed between modeled and measured responses across all switching states, with minor deviations attributed to fabrication tolerances and measurement setup limitations. Table 3 offers a comparative analysis between the proposed filtenna and a recently reported design. The results confirm that the proposed structure offers a more compact size, broader tunable frequency range, and the practical advantage of employing mechanical switches.

5. DESIGN OF THE MIMO FILTENNA

To enhance the reliability of wireless communication links, diversity techniques are employed whereby duplicated data is transmitted through multiple, independently fading channels.

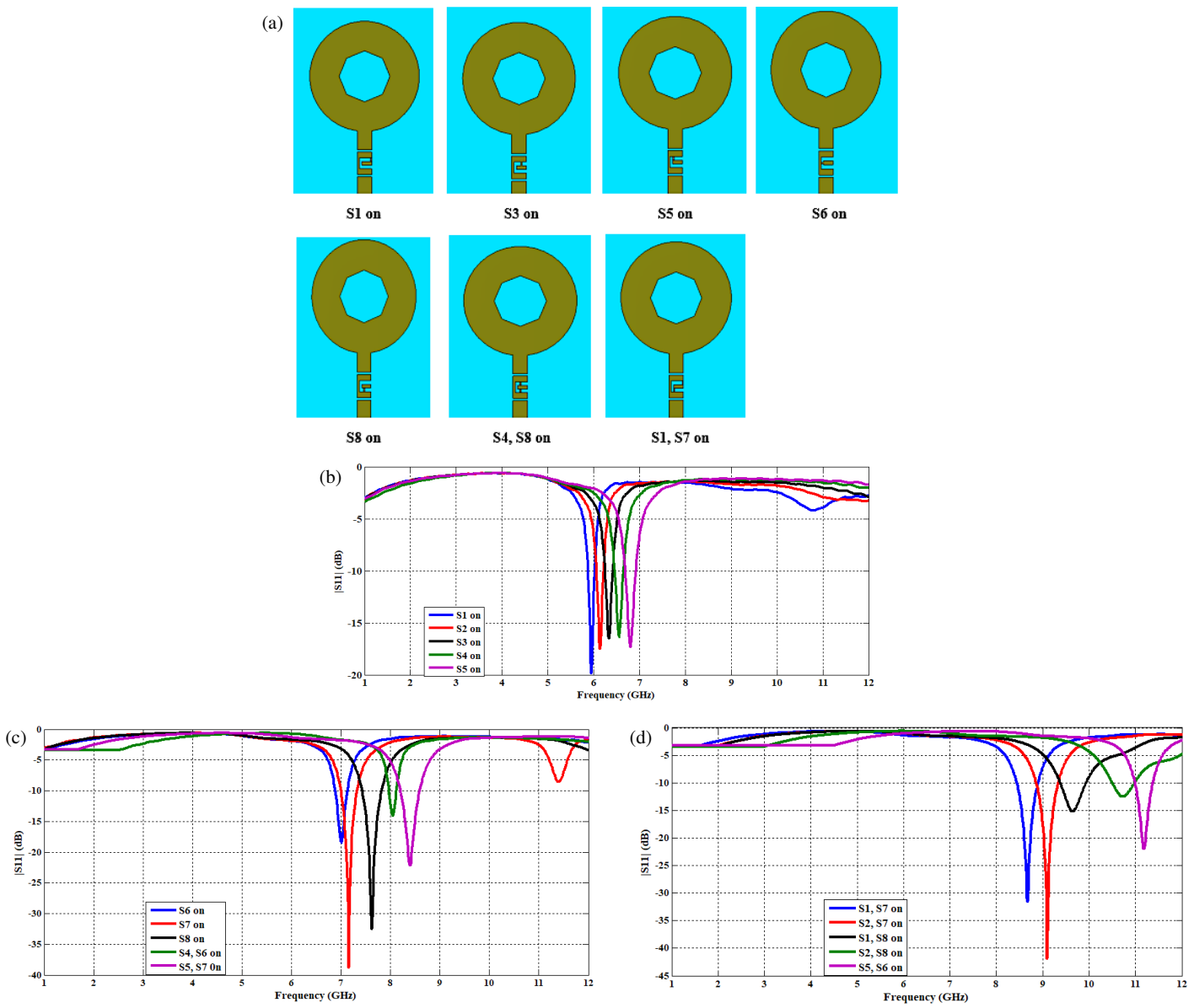

FIGURE 11. (a) Various shapes of switching states, and Reflection coefficient ($|S_{11}|$) of the proposed filtenna under various switching states when (b) S1, S2 S3, S4, S5 are on, (c) S6, S7, S8, S4 and S6, S5 and S7 are on, (d) S1 and S7, S2 and S7, S1 and S8, S2 and S8, S5 and S6 are on.

All switchs off | S1 on | S1 and S7 on | S4, S6 on

FIGURE 12. Fabricated model of the proposed filtenna under different mechanical switch configurations. The switches are implemented using manually inserted metallic screws placed at designated points on the filter structure. Each configuration shown corresponds to a specific screw activation state that enables frequency tuning by altering the current path in the feed network.

TABLE 3. Performance comparison between the planned filtenna and present designs from literature.

Refs	Working frequency span (GHz)	Selectable frequency span (GHz)	Dimensions (mm^2)	Material of substrat	Tuning mechanism
[35]	3.38 and 5.37 (dual-band)	2.0	30 × 30	FR-4	Varactor diode (BB833)
[36]	2.0–6.0	3.8	50 × 45	FR-4	Two PIN diodes
[37]	2.95–5.16	2.21	50 × 50	FR-4	Mechanical switches (adjustable screws)
[38]	3.5–4.65	1.15	40 × 40	FR-4	Single varactor diod
[39]	1.375–5.825	4.45	41 × 41	FR-4	Single varactor diod
[40]	2.2–5.5	3.3	50 × 40	FR-4	PIN + varactor diode
Planned filtenna	Covering frequencies from 5.9 GHz up to and exceeding 12 GHz	5.55	45 × 35	FR-4	Mechanically switche

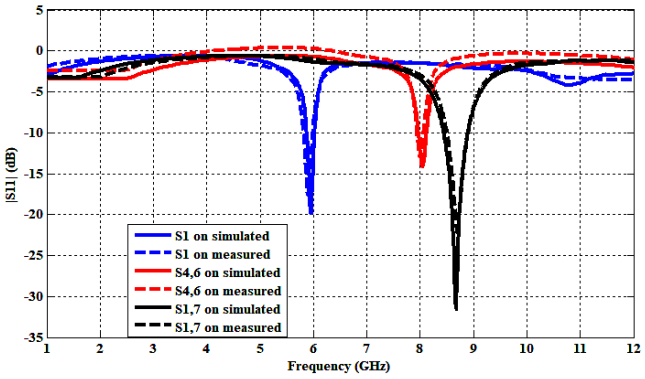

FIGURE 13. Evaluation of $|S_{11}|$ characteristics for the filtenna in different switch states: simulation and measurement comparison.

This approach allows for improved signal robustness once the received signals are appropriately combined. Utilizing antennas with diversity capabilities in such systems contributes to better channel quality and increased data throughput. This section presents a frequency-tunable MIMO filtenna designed to support pattern diversity. As shown in Figure 14(a), the configuration consists of two filtenna elements mounted orthogonally within a compact layout measuring 80 mm × 45 mm. The orthogonal positioning helps reduce mutual interference between the elements, which is critical for effective MIMO performance. Ports 1 and 2 are used as the excitation terminals, and the design ensures that MC between them, denoted as S_{xy}, $x, y = 1, 2$, $x \neq y$, remains minimal. Figure 14(b) illustrates the simulated S-parameters of the MIMO filtenna without any additional decoupling structure. At the resonance frequency of 7.6 GHz, the reflection coefficient (S_{11}) reaches −45 dB, while the isolation (S_{11}) is maintained at −40 dB, indicating strong isolation and minimal coupling between the ports.

6. RESULTS AND DISCUSSION

Figure 15 visually demonstrates the outward current spreading on the planned MIMO antenna elements without decoupling structure (DS). Figure 15(a) visualizes the surface current when input is applied to Port 1. A clear and strong concentration of current density is observed primarily around the fed element of Port 1 and its immediate radiating structure. Crucially, the current magnitude on the adjacent, unexcited Port 2 remains very low, indicating minimal electromagnetic coupling. Similarly, Figure 15(b) visualizes the surface current when input is applied to Port 2. In this case, the high current density is concentrated around Port 2's feeding point and its radiating parts, while Port 1 exhibits significantly reduced current.

The fundamental concept behind the proposed decoupling structure (DS) involves integrating a metamaterial-based element — resembling a balloon-like geometry — comprising eight circular resonators, each with a radius of 2.5 mm and a total length of 22.5 mm. This assembly is embedded between the two antennas to mitigate MC by suppressing undesired electromagnetic interaction. To optimize space utilization and enhance isolation, a high-impedance transmission line is implemented in a meandered (balloon-shaped) configuration, as illustrated in Figure 16.

Figure 17 presents a comparative analysis of the MC between antenna elements, both with and without the integration of a DS. MC, expressed in decibels (dB), is a critical parameter for MIMO antenna systems, as lower values indicate better isolation between radiating elements, leading to improved diversity performance and reduced interference. A significant reduction in MC is evident across the entire operational band when the DS is present. For instance, at the working frequency of 7.6 GHz, the MC is notably lower with the DS (approximately −45 dB) compared to the scenario without it (approximately −30 dB). This substantial improvement, particularly in the lower MC achieved with the DS, confirms its effectiveness in enhancing the isolation between the antennas. This superior isolation is crucial for maximizing the efficiency and performance of MIMO systems by mitigating signal distortion and increasing channel capacity.

Figure 18 visualizes the surface current behavior of the developed MIMO filtenna at 7.6 GHz, highlighting key aspects

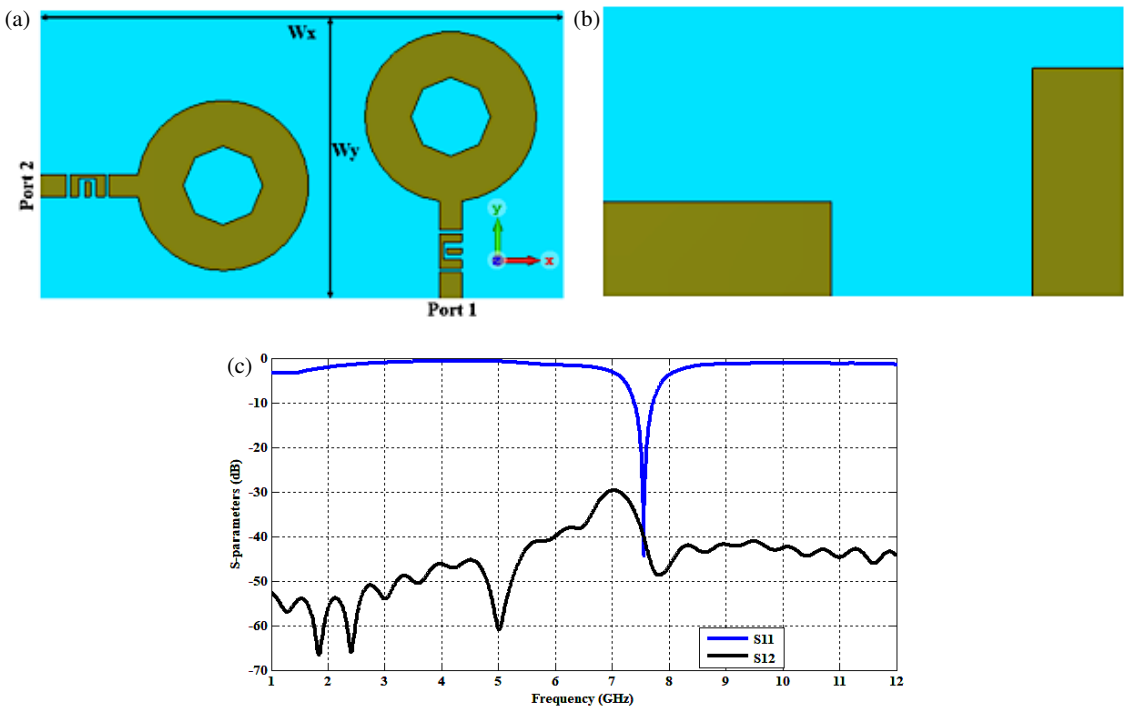

FIGURE 14. Shape of the planned MIMO filtenna without DS: (a) top view, (b) bottom view, and (c) simulated S-parameters.

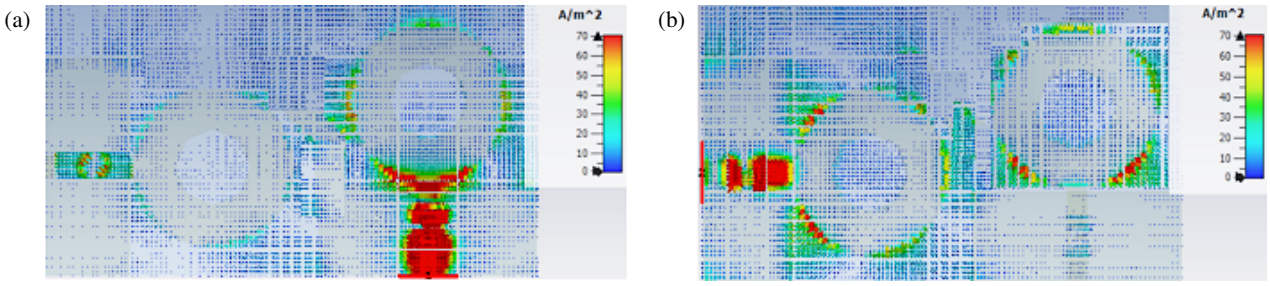

FIGURE 15. Surface current distribution of the MIMO filtenna elements under excitation: (a) port 1 active, (b) port 2 active.

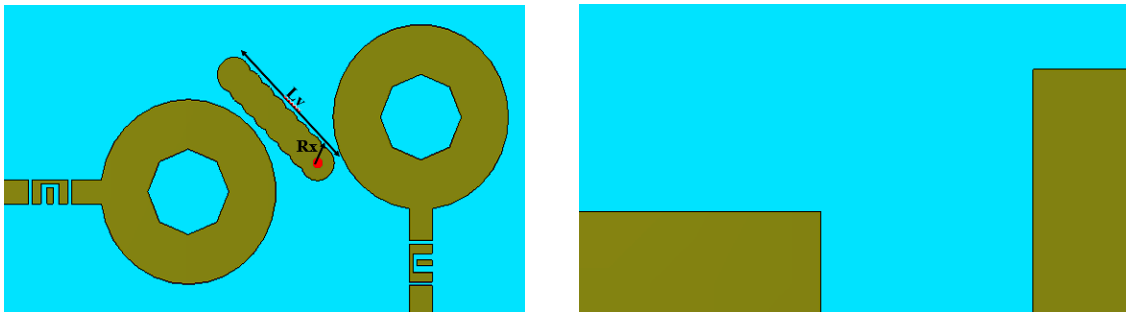

FIGURE 16. Structural layout of the planned MIMO filtenna incorporating the (DS), with overall dimensions $W_{\text{MIMO}} = 80\,\text{mm}$, $L_{\text{MIMO}} = 45\,\text{mm}$, and $W_z = L_z = 2.5\,\text{mm}$.

of its function and inter-element isolation. Specifically, in Figure 18(a), the distribution is shown under excitation at Port 1.

A clear concentration of high current density is observed around the feeding point of Port 1 and extends along its radiating elements. Crucially, the current distribution on the unexcited Port 2 remains very low, demonstrating excellent isolation between the antenna elements. Similarly, Figure 18(b) depicts that the distribution is shown under excitation at Port 2. Here, high current density is concentrated around the feeding point of Port 2 and its corresponding radiating structure, while Port 1 exhibits minimal current activity. The distinct and localized current distributions in both scenarios confirm that the

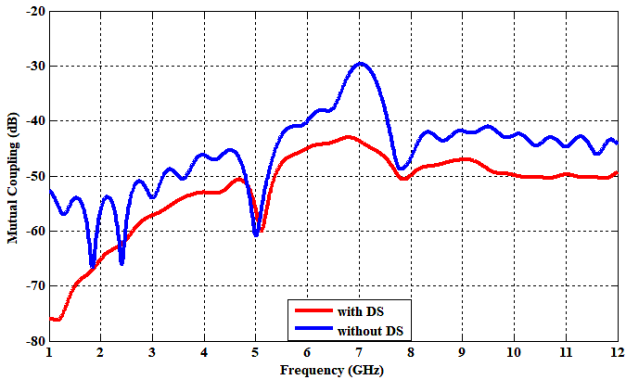

FIGURE 17. MC levels between MIMO filtenna elements with and without the DS.

two antenna elements are largely independent and exhibit low MC. This effective isolation, visually confirmed by the current distribution patterns, is a critical factor for achieving high diversity gain and robust performance in MIMO systems, as it minimizes interference between individual antenna channels.

6.1. Performance Assessment of the MIMO Filtenna Design

6.1.1. Envelop Correlation Coefficient (ECC)

In a MIMO scheme, the level of correlation between elements can be quantified using ECC. This parameter provides insight into how independently the antennas operate within the system. ECC is typically estimated based on scattering parameters S_{ij} and S_{ji}. For a MIMO configuration to achieve high performance and spatial diversity, the ECC value should ideally remain below 0.5 [38, 40]. The following expression is commonly used to approximate ECC from S-values [41]:

$$ECC = \frac{\left|S_{11}^{*}S_{12} + S_{21}^{*}S_{22}\right|^{2}}{\left(1 - \left|S_{11}\right|^{2} + \left|S_{21}\right|^{2}\right)\left(1 - \left|S_{22}\right|^{2} + \left|S_{12}\right|^{2}\right)}$$

6.1.2. Diversity Gain (DG)

DG is an indicator for the diversity level. A high value is needed for effective isolation. (5) [42] can be used to evaluate it.

$$DG = \sqrt{1 - ECC^{2}}$$

6.1.3. Total Active Reflection Coefficient (TARC)

TARC reflects the efficiency of a multi-port antenna in handling signals when multiple ports are simultaneously active. It is computed by taking the ratio between the reflected and incident power in root form, as expressed in Equation (6) [43, 44].

$$\Gamma_{a}^{t} = \frac{\sqrt{\left|(S_{11} + S_{12}e^{j\theta})\right|^{2} + \left|(S_{21} + S_{22}e^{j\theta})\right|^{2}}}{2}$$

6.2. Manufacture and Measurement

Figure 19(a) presents the realized prototype of the developed MIMO filtenna. Figure 20 provides an evaluation of the imitation and measured performance of the antenna, focusing on two key parameters: VSWR and S-parameters. Figure 20(a) presents the voltage standing wave ratio (VSWR) as a function of frequency. The antenna exhibits a low VSWR, particularly around 7.6 GHz, indicating good impedance matching at this operating frequency as clear in Figure 20(a). Figure 20(b) displays the scattering parameters of MIMO antennas. A key observation is the significantly low reflection coefficients at the operating frequency, implying efficient power transfer. Furthermore, the MC (S_{12} and S_{21}) remains low across the operational band, which is essential for ensuring good isolation between the antenna elements in a MIMO filtenna, minimizing interference and enabling better data throughput. The strong concordance between the simulated and measured values validates the accuracy of the antenna's design and predictive models.

Figure 21 presents the beam forms of the planned MIMO filtenna at 7.6 GHz. Specifically, Figure 21(a) illustrates the y-z plane beam form, where a strong directional beam is observed, indicating the antenna's capability to focus radiated power in a certain track. A high level of consistency is observed between the imitation and experimental outcomes in both form and behavior.

Magnitude validates the antenna's design and act in this plane. Concurrently, Figure 21(b) displays the x-y plane beam form, revealing a more omnidirectional characteristic with multiple lobes, suggesting broader coverage in the horizontal plane. Again, the simulated and measured results show good correlation, reinforcing the reliability of the antenna's act across different orientations. These patterns collectively demonstrate the filtenna's effectiveness in achieving desired radiation characteristics for MIMO applications at 7.6 GHz.

Figure 22 provides a comprehensive evaluation of the proposed MIMO filtenna's performance by illustrating its gain and efficiency characteristics across a range of frequencies. Figure 22(a) depicts the gain (dBi) versus frequency, demonstrating that the antenna accomplishes a peak gain of nearly 6 dBi around 7.6 GHz, which is a wanted characteristic for effective signal transmission and response. Figure 22(b) presents the antenna's efficiency as a function of frequency. The plot reveals that the filtenna maintains high efficiency, reaching a maximum around 80% near 7.6 GHz, indicating minimal power loss within the antenna structure.

Figure 23 presents a inclusive evaluation of the projected MIMO antenna's performance through key diversity metrics: ECC, DG, and TARC. Figure 23(a) illustrates the ECC, which quantifies the correlation between the beam shapes of the MIMO elements. Ideally, ECC values should be close to zero for optimal diversity performance. The ECC remains consistently low across the operational frequency band, especially under 0.003, signifying excellent isolation and minimal correlation between the antenna elements. This low ECC is crucial for maximizing the diversity gain and improving the reliability of MIMO communication. Figure 23(b) displays the DG, which

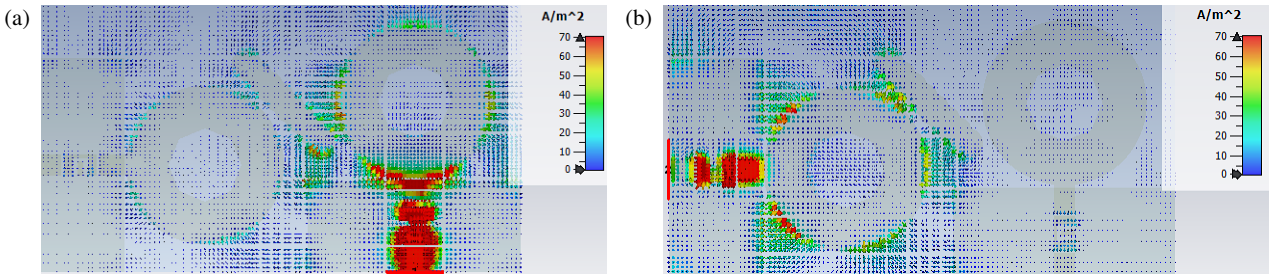

FIGURE 18. Simulated current spreading at 7.6 GHz for the planned MIMO filtenna when excited through (a) Port 1 and (b) Port 2.

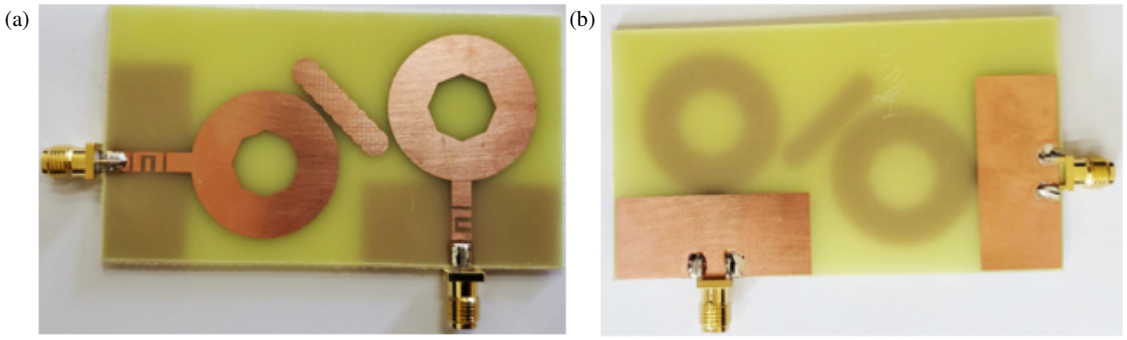

FIGURE 19. Fabricated MIMO filtenna. (a) Front side (b) back side.

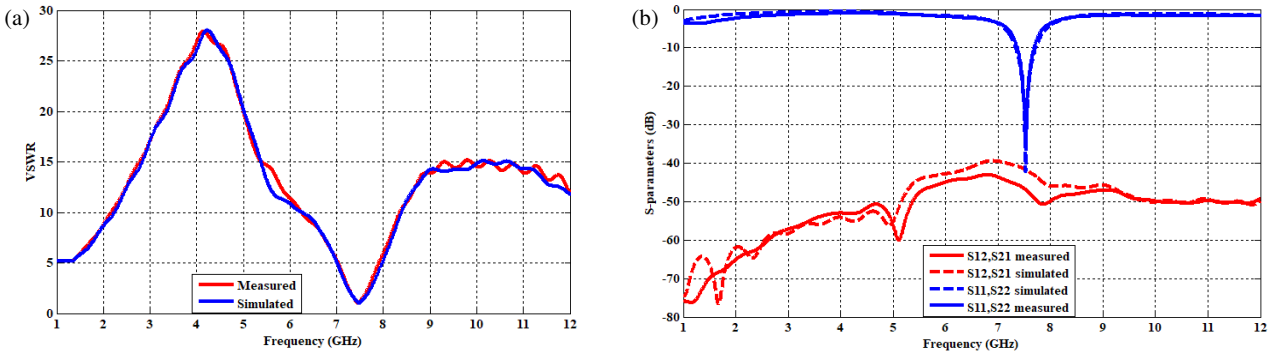

FIGURE 20. Simulated and measured results: (a) (VSWR), and (b) scattering parameters (S-parameters).

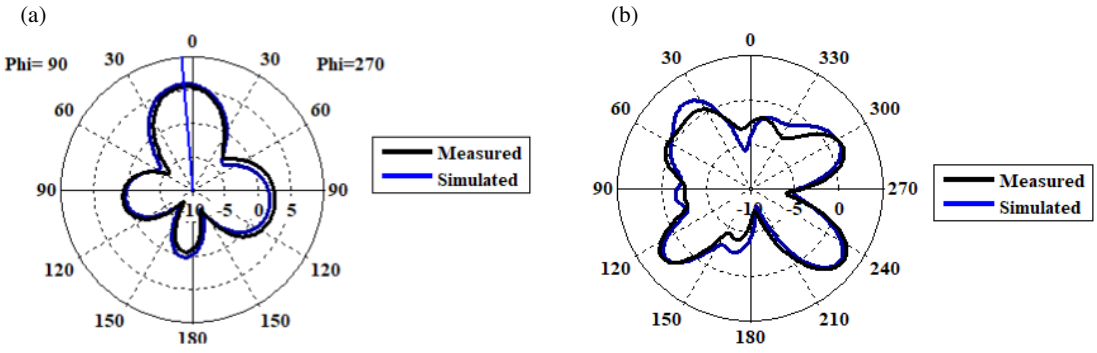

FIGURE 21. Beam patterns of the proposed MIMO filtenna at 7.6 GHz: (a) in the y-z plane, and (b) in the x-y plane.

measures the advance in signal-to-noise ratio accomplished by using a diversity antenna system compared to a single antenna. Values close to 10 dB signify ideal diversity performance. Figure 23(b) demonstrates that the DG is consistently high, near 9.998 dB, across the frequency range, reinforcing the antenna's robust diversity capabilities. Finally, Figure 23(c) shows the TARC, which assesses the collective reflection of all antenna ports under realistic operating conditions. A low TARC indicates good impedance matching and efficient power transfer for the entire MIMO system. The graph reveals that the TARC re-

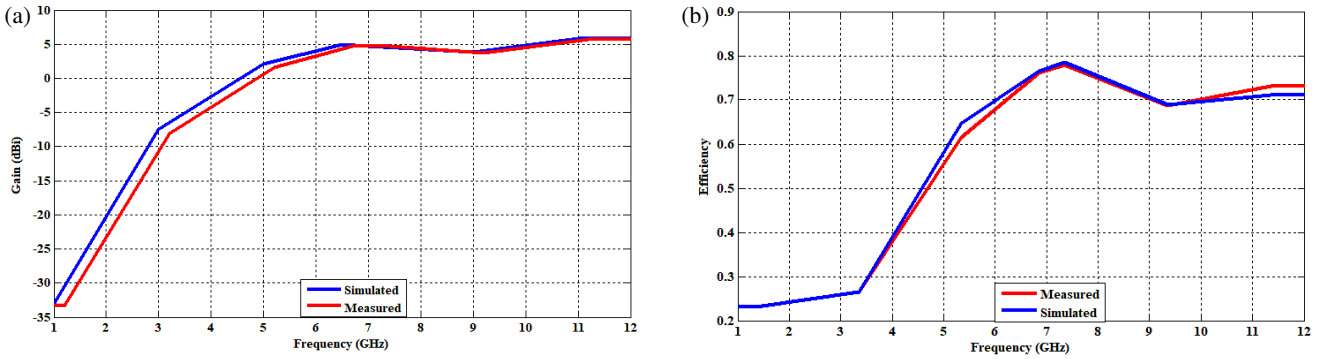

FIGURE 22. Results of (a) gain and (b) efficiency of planned MIMO filtenna.

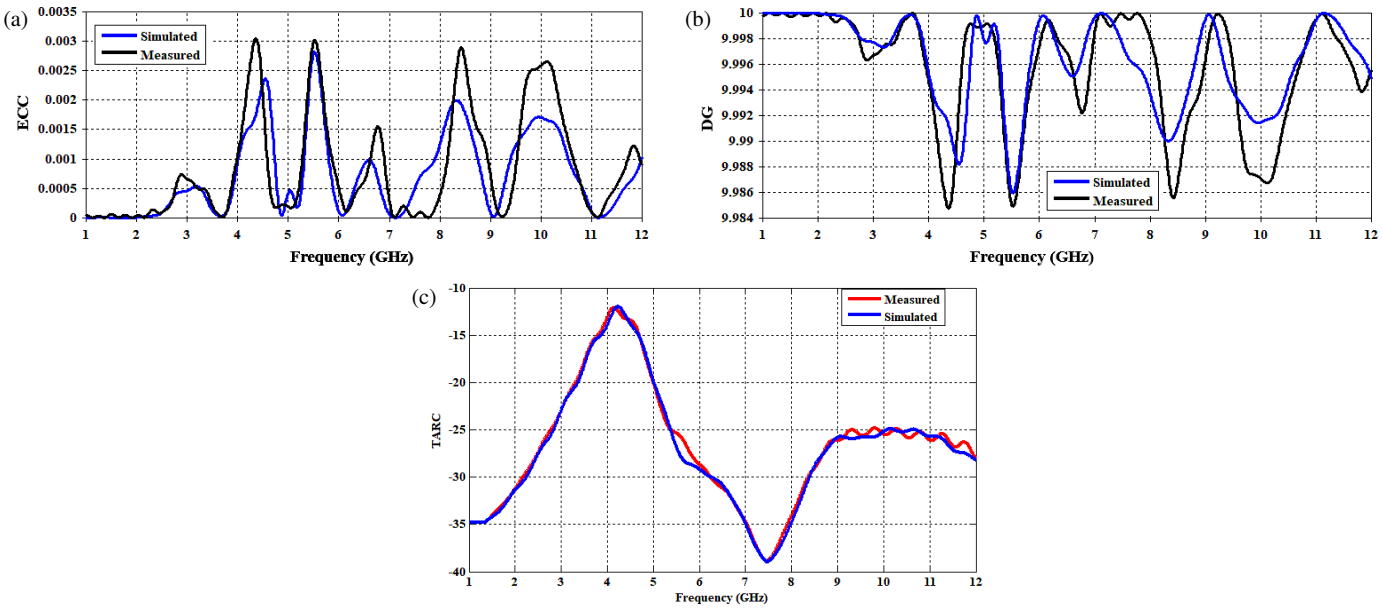

FIGURE 23. MIMO constraints (a) ECC, (b) DG and (c) TARC.

TABLE 4. Benchmarking the planned MIMO filtenna against related studies in the literature.

Ref.	Dimensions (mm^2)	No of Ports	Bandwidth (GHz)	ECC	DG	MC	Gain (dBi)
[26]	65×50	2	1.2–6	0.1	9.96	-25	< 4
[31]	55×60	2	3.4–3.5	—	—	-20	5.8
[42]	75.2×75.2	4	3.1–17.3	0.1	—	-14.5	5.5
[43]	32×64	2	3.1–10.6	< 0.02	—	-17	4
[45]	178×178	4	2.7–4.9	~ 0.001	~ 1	< -25	6.3
[46]	150×80	8	2.4, 3.5, 5.5	< 0.0	9.98	17.5	4
[47]	78×64.5	4	$\sim$ 3.3–3.8	0.0078	9.96	-22	4.4
Planed work	$2\ 80 \times 45$	2	7.4–7.75 GHz	< 0035	9.998	-48	6

mains below -10 dB crossways the frequency band, signifying excellent overall impedance matching and minimal signal reflection.

7. COMPARISON WITH PREVIOUS WORK

Table 4 demonstrates a comparative analysis between the projected antenna and existing designs in the literature and reveals the advantages of the planned configuration in standings of size, bandwidth, ECC, DG, MC, and gain. For instance, the antenna in [26] offers a widespread bandwidth of 1.2–6 GHz with an ECC of 0.1 and a gain below 4 dBi, while [31] achieves a narrower bandwidth (3.45–3.55 GHz) but slightly higher gain at 5.8 dBi. Ref. [42] presents a four-port MIMO system covering an ultra-wideband range (3.1–17.3 GHz), yet the ECC remains at 0.1, and gain is limited to 5.5 dBi. Similarly, [43]

achieves a broader bandwidth of 3.1–10.6 GHz with low ECC (< 0.02), but the gain does not exceed 4 dBi. In contrast, larger MIMO systems like in [45] and [46] offer improved DG ($\sim$ 10 dB) and moderate gains (up to 6.3 dBi), but they require substantially larger form factors ($178 \times 178\,\text{mm}^2$ and $150 \times 80\,\text{mm}^2$, respectively). The design in [47] achieves good isolation (-22 dB) and acceptable gain (4.4 dBi), but with limited bandwidth ($\sim$ 3.3–3.8 GHz). Compared to them, the proposed two-port antenna exhibits superior isolation (-48 dB), excellent ECC (< 0.0035), high DG (9.998 dB), and improved gain (6 dBi), all within a compact footprint of $80 \times 45\,\text{mm}^2$ and a focused operational bandwidth of 7.4–7.75 GHz, demonstrating its potential for high-performance compact MIMO applications.

8. CONCLUSION

A mechanically reconfigurable filtenna has been successfully developed, offering both wideband and highly selective narrowband operation suitable for sub-6 GHz and X-band applications. By embedding a DMS-based BPF within the feedline of a compact circular patch antenna, reconfigurability is realized through mechanical switching, achieving discrete frequency tuning with minimal complexity and cost. The planned two-port MIMO configuration, enhanced with a metamaterial decoupling structure, delivers exceptional isolation, low ECC, and high diversity performance within a miniaturized form factor. Measured outcomes approve the simulation predictions, demonstrating the antenna's suitability for adaptive and compact wireless communication schemes. This design bridges the gap between compactness and functionality, paving the way for flexible RF front-end architectures in next-generation wireless platforms.

ACKNOWLEDGEMENT

The authors would like to thank Universiti Teknikal Malaysia Melaka (UTeM) and the Ministry of Higher Education (MOHE) of Malaysia for supporting this project.

REFERENCES

[1] Rawat, S., H. Singh, and M. Kumar, "Design and analysis of compact reconfigurable filtenna using DMS for multi-band wireless applications," *IEEE Access*, Vol. 12, 48 032–48 043, 2024.

[2] Prashad, L., H. C. Mohanta, and A. J. A. Al-Gburi, "Dual band rectenna for electromagnetic energy harvesting at 2.4 GHz and 5 GHz frequencies," *Progress In Electromagnetics Research B*, Vol. 108, 75–88, 2024.

[3] Marzouk, M., I. H. Nejdi, Y. Rhazi, M. Saih, J. A. Nasir, A. Daher, M. Hussein, Z. Zakaria, and A. J. A. Al-Gburi, "Low-profile reconfigurable UWB fractal antenna enhanced by parasitic elements for wireless applications," *Progress In Electromagnetics Research Letters*, Vol. 126, 37–48, 2025.

[4] El Aoud, S. E., H. Abbaoui, O. Benkhadda, S. Attioui, N. E. Assri, S. Ibnyaich, A. Zeroual, M. M. Ismail, and A. J. A. Al-Gburi, "Design of a crescent moon-shaped reconfigurable patch antenna using a PIN diode for 5G sub-6 GHz and multistandard wireless applications," *Progress In Electromagnetics Research B*, Vol. 109, 81–93, 2024.

[5] Chinda, F. E., M. Hanif, S. Soeung, M. S. Yahya, A. J. A. Al-Gburi, F. Bashir, F. Zahoor, and C. Sovuthy, "Design of sub-6 GHz BPF using chained even and odd mode admittance polynomials for 5G C-band applications," *Results in Engineering*, Vol. 25, 103614, 2025.

[6] Awan, W. A., N. Hussain, S. Kim, and N. Kim, "A frequency-reconfigurable filtenna for GSM, 4G-LTE, ISM, and 5G Sub-6 GHz band applications," *Sensors*, Vol. 22, No. 15, 5558, 2022.

[7] Liu, H., P. Wen, S. Zhu, B. Ren, X. Guan, and H. Yu, "Quad-band CPW-fed monopole antenna based on flexible pentangle-loop radiator," *IEEE Antennas and Wireless Propagation Letters*, Vol. 14, 1373–1376, 2015.

[8] Kumar, A., G. Singh, M. K. Abdulhameed, S. R. Hashim, and A. J. A. Al-Gburi, "Development of fractal 5G MIMO antenna for sub 6 GHz wireless automotive applications," *Progress In Electromagnetics Research M*, Vol. 130, 121–128, 2024.

[9] Elabd, R. H. and A. J. A. Al-Gburi, "Low mutual coupling miniaturized dual-band quad-port MIMO antenna array using decoupling structure for 5G smartphones," *Discover Applied Sciences*, Vol. 6, No. 4, 189, 2024.

[10] El-abd, R. H., H. H. Abdullah, M. A. Elazim, and A. S. Samrah, "Low complexity high-performance precoding algorithms for mm-Wave MU-MIMO communication system," *Wireless Personal Communications*, Vol. 115, No. 3, 2489–2500, 2020.

[11] Elabd, R. H. and A. J. A. Al-Gburi, "SAR assessment of miniaturized wideband MIMO antenna structure for millimeter wave 5G smartphones," *Microelectronic Engineering*, Vol. 282, 112098, 2023.

[12] Al Gburi, A. J. A., "5G MIMO antenna: Compact design at 28/38 GHz with metamaterial and SAR analysis for mobile phones," *Przegląd Elektrotechniczny*, Vol. 2024, No. 4, 171–174, 2024.

[13] Mistri, R. K., S. K. Mahto, A. K. Singh, R. Sinha, A. J. A. Al-Gburi, T. A. H. Alghamdi, and M. Alathbah, "Quad element MIMO antenna for C, X, Ku, and Ka-band applications," *Sensors*, Vol. 23, No. 20, 8563, 2023.

[14] Al-Gburi, A. J. A., I. B. M. Ibrahim, Z. Zakaria, and N. F. B. M. Nazli, "Wideband microstrip patch antenna for sub 6 GHz and 5G applications," *Przegląd Elektrotechniczny*, Vol. 97, No. 11, 26–29, 2021.

[15] Benkhadda, O., M. Saih, A. Reha, S. Ahmad, K. Chaji, H. Singh, and A. J. A. Al-Gburi, "A miniaturized reconfigurable antenna for modern wireless applications with broadband and multi-band capabilities," *Progress In Electromagnetics Research M*, Vol. 127, 93–101, 2024.

[16] Perli, B. R., T. Addepalli, G. Divya, M. K. Kumar, M. Sharma, C. Raju, and A. J. A. Al-Gburi, "Serpent-configured quad-port MIMO antenna with dual-band operation and defected substrate-ground structure for millimeter-wave systems," *Journal of Infrared, Millimeter, and Terahertz Waves*, Vol. 46, No. 7, 43, 2025.

[17] Guariglia, E., "Harmonic sierpinski gasket and applications," *Entropy*, Vol. 20, No. 9, 714, 2018.

[18] Guariglia, E. and R. C. Guido, "Chebyshev wavelet analysis," *Journal of Function Spaces*, Vol. 2022, No. 1, 5542054, 2022.

[19] Sibille, A., C. Oestges, and A. Zanella, *MIMO: From Theory to Implementation*, 1st ed., Academic Press, Diego, CA, USA, 2010.

[20] Elabd, R. H., A. J. A. Al-Gburi, and A. A. Megahed, "Compact circular MIMO antenna with defected ground structure (DGS) for improved isolation in 5G sub-6 GHz mobile systems," *Results in Engineering*, Vol. 27, 105737, 2025.

[21] Reha, A., O. Benkhadda, A. O. Said, A. E. Amri, and A. J. A. Al-Gburi, "Design of sub-6 GHz and sub-7 GHz dragon fractal antenna for 5G applications with enhanced bandwidth," *International Journal of Intelligent Engineering & Systems*, Vol. 18, No. 2, 14–22, 2025.

[22] Elabd, R. H., H. H. Abdullah, and M. Abdelazim, "Compact highly directive MIMO vivaldi antenna for 5G millimeter-wave base station," *Journal of Infrared, Millimeter, and Terahertz Waves*, Vol. 42, No. 2, 173–194, 2021.

[23] Kumar, P., A. K. Singh, R. Kumar, R. Sinha, S. K. Mahto, A. Choubey, and A. J. A. Al-Gburi, "High isolated defected ground structure based elliptical shape dual element MIMO antenna for S-band applications," *Progress In Electromagnetics Research C*, Vol. 143, 67–74, 2024.

[24] Jetti, C. R., T. Addepalli, S. R. Devireddy, G. K. Tanimki, A. J. A. Al-Gburi, Z. Zakaria, and P. Sunitha, "Design and analysis of modified U-shaped four element MIMO antenna for dual-band 5G millimeter wave applications," *Micromachines*, Vol. 14, No. 8, 1545, 2023.

[25] Thakur, E., N. Jaglan, A. Gupta, and A. J. A. Al-Gburi, "Multi-band notched circular polarized MIMO antenna for ultra-wideband applications," *Progress In Electromagnetics Research M*, Vol. 125, 87–95, 2024.

[26] Pahadsingh, S. and S. Sahu, "An integrated MIMO filtenna with wide band-narrow band functionality," *AEU — International Journal of Electronics and Communications*, Vol. 110, 152862, Oct. 2019.

[27] Masoodi, I. S., I. Ishteyaq, K. Muzaffar, and M. I. Magray, "A compact band-notched antenna with high isolation for UWB MIMO applications," *International Journal of Microwave and Wireless Technologies*, Vol. 13, No. 6, 634–640, Jul. 2021.

[28] Dkiouak, A., A. Zakriti, M. E. Ouahabi, and A. Mchbal, "Design of two element Wi-MAX/WLAN MIMO antenna with improved isolation using a short stub-loaded resonator (SSLR)," *Journal of Electromagnetic Waves and Applications*, Vol. 34, No. 9, 1268–1282, 2020.

[29] Hassan, M. M., M. Rasool, M. U. Asghar, Z. Zahid, A. A. Khan, I. Rashid, A. Rauf, and F. A. Bhatti, "A novel UWB MIMO antenna array with band notch characteristics using parasitic decoupler," *Journal of Electromagnetic Waves and Applications*, Vol. 34, No. 9, 1225–1238, 2020.

[30] Li, Z., Z. Du, M. Takahashi, K. Saito, and K. Ito, "Reducing mutual coupling of MIMO antennas with parasitic elements for mobile terminals," *IEEE Transactions on Antennas and Propagation*, Vol. 60, No. 2, 473–481, Feb. 2012.

[31] Abdullah, M., Q. Li, W. Xue, G. Peng, Y. He, and X. Chen, "Isolation enhancement of MIMO antennas using shorting pins," *Journal of Electromagnetic Waves and Applications*, Vol. 33, No. 10, 1249–1263, 2019.

[32] Luo, S., Y. Li, Y. Xia, and L. Zhang, "A low mutual coupling antenna array with gain enhancement using metamaterial loading and neutralization line structure," *Applied Computational Electromagnetics Society Journal (ACES)*, Vol. 34, No. 3, 411–418, Mar. 2019.

[33] Yuan, X.-T., W. He, K.-D. Hong, C.-Z. Han, Z. Chen, and T. Yuan, "Ultra-wideband MIMO antenna system with high element-isolation for 5G smartphone application," *IEEE Access*, Vol. 8, 56 281–56 289, 2020.

[34] Lin, G.-S., C.-H. Sung, J.-L. Chen, L.-S. Chen, and M.-P. Houng, "Isolation improvement in UWB MIMO antenna system using carbon black film," *IEEE Antennas and Wireless Propagation Letters*, Vol. 16, 222–225, 2017.

[35] Shah, S. M., K. Hamdan, Z. Z. Abidin, F. C. Seman, S. A. Hamzah, N. Katiran, and F. Zubir, "Frequency tuning varactor-loaded reconfigurable antenna for m-WiMAX and WLAN applications," *Indonesian Journal of Electrical Engineering and Computer Science*, Vol. 13, No. 2, 779–786, Feb. 2019.

[36] Abdulraheem, Y. I., G. A. Oguntala, A. S. Abdullah, H. J. Mohammed, R. A. Ali, R. A. Abd-Alhameed, and J. M. Noras, "Design of frequency reconfigurable multiband compact antenna using two PIN diodes for WLAN/WiMAX applications," *IET Microwaves, Antennas & Propagation*, Vol. 11, No. 8, 1098–1105, Jun. 2017.

[37] Mariem, M. and G. Ali, "Designs of frequency reconfigurable planar bow-tie antenna integrated with PIN, varactor diodes and parasitic elements," *Advances in Science, Technology and Engineering Systems Journal*, Vol. 6, No. 4, 320–326, 2021.

[38] Al Ahmad, M., S. Kabeer, A. A. Sanad, and L. J. A. Olule, "Compact single-varactor diode frequency-reconfigurable microstrip patch antenna," *IET Microwaves, Antennas & Propagation*, Vol. 15, No. 9, 1100–1107, Jul. 2021.

[39] Dildar, H., F. Althobiani, I. Ahmad, W. U. R. Khan, S. Ullah, N. Mufti, S. Ullah, F. Muhammad, M. Irfan, and A. Glowacz, "Design and experimental analysis of multiband frequency reconfigurable antenna for 5G and sub-6 GHz wireless communication," *Micromachines*, Vol. 12, No. 1, 32, 2021.

[40] El Mustapha Iftissane, M. D. B., S. Bri, J. Foshi, and N. Jebbor, "Design and analysis of frequency reconfigurable antenna embedding varactor diodes," *Advances in Science, Technology and Engineering Systems Journal*, Vol. 4, No. 6, 371–376, 2019.

[41] Ahmad, I., H. Dildar, W. U. R. Khan, S. Ullah, S. Ullah, M. A. Albreem, M. H. Alsharif, and P. Uthansakul, "Frequency reconfigurable antenna for multi standard wireless and mobile communication systems," *Computers, Materials & Continua*, Vol. 68, No. 2, 2563–2578, 2021.

[42] Kayabasi, A., A. Toktas, E. Yigit, and K. Sabanci, "Triangular quad-port multi-polarized UWB MIMO antenna with enhanced isolation using neutralization ring," *AEU — International Journal of Electronics and Communications*, Vol. 85, 47–53, Feb. 2018.

[43] Kumar, N. and K. U. Kiran, "Meander-line electromagnetic bandgap structure for UWB MIMO antenna mutual coupling reduction in *E*-plane," *AEU — International Journal of Electronics and Communications*, Vol. 127, 153423, Dec. 2020.

[44] Kumar, P., A. K. Singh, R. Kumar, S. K. Mahto, P. Pal, R. Sinha, A. Choubey, and A. J. A. Al-Gburi, "Design and analysis of low profile stepped feedline with dual circular patch mimo antenna and stub loaded partial ground plane for wireless applications," *Progress In Electromagnetics Research C*, Vol. 140, 135–144, 2024.

[45] Salehi, M. and H. Oraizi, "Wideband high gain metasurface-based 4T4R MIMO antenna with highly isolated ports for sub-6 GHz 5G applications," *Scientific Reports*, Vol. 14, No. 1, 14448, Jun. 2024.

[46] Lumina, A. V., S. Manoharan, and S. Kumar, "Eight-port multiband MIMO antenna design with high isolation for 5G smartphones," *International Journal of Microwave and Wireless Technologies*, Vol. 16, No. 8, 1316–1330, 2024.

[47] Srinubabu, M. and N. V. Rajasekhar, "Design and analysis of a compact 4-Port MIMO antenna for improved isolation and 5G (n78/n77/n48) Performance," *Traitement du Signal*, Vol. 41, No. 4, 2057–2067, Aug. 2024.